

OPTIMIZATION OF MORPHOLOGICAL AND KINEMATIC PARAMETER FOR FLAPPING WING IN FORWARD FLIGHT

Xue Dong[1], Gao Yating[2], Wu Tao[3], Song Bifeng[4] & Song Wenping[5]

[1]Northwestern Polytechnical University, Xi'an 710072, China
[2]Northwestern Polytechnical University, Xi'an 710072, China
[3]Northwestern Polytechnical University, Xi'an 710072, China
[4]Northwestern Polytechnical University, Xi'an 710072, China
[5]Northwestern Polytechnical University, Xi'an 710072, China\

Abstract

The paper conducted a optimization of morphological and kinematic parameters of flapping wings, based on the CFD method and surrogate optimization model. The optimization model considered the complex motion parameters of birds, including the proportion of flapping time, flapping, sweeping, and passive twisting, and the planar shape was divided into two segments to make the morphology and motion closer to the real geometric and motion patterns of birds. Ultimately, a flapping wing with an average thrust coefficient increase of 0.138 (equivalent to an increase in thrust of 17.8 g per wing)was obtained. The increase in mean thrust coefficient of the flapping wing was mainly due to the larger downward tilting and twisting motion during the downstroke. The improvement in lift performance of the optimized wing is 32.6% and is mainly due to the coupling of the upward tilting and twisting motion during the upstroke phase with the longer upstroke time. The optimization model provides a useful tool for the design of complex motion and planar shapes of bird-inspired FWMAVs, promoting further improvement of the aerodynamic performance of flapping wings.

Keywords: Optimization,Flapping wing

1.Introduction

Inspired by avian flight in nature, bird-inspired Flapping-Wing Micro Aerial Vehicles (FWMAVs) have achieved success and attracted widespread attention. In recent years, various countries have invested a great deal of manpower and resources in researching bionic flapping flight and have successfully developed several types of FWMAVs. However, there is still a lot of room for improvement in flight performance. For example, the flapping motion of small and medium-sized birds is complex, including typical movements such as flapping, twisting, sweeping, and folding. Birds often achieve maximum aerodynamic efficiency during their cruising phase and maximum aerodynamic force during slow flight by coupling and coordinating these different movements. However, most small and medium-sized FWMAVs[1][2], as shown in the Figure 1, use a flapping motion pattern of single degree of freedom flapping and passive twisting and adopt relatively simple planar shapes, which is far less efficient and effective than flying creatures in nature, and requires further optimization design in the morphological and kinematic parameter.



Figure 1 Some bird-inspired Flapping-Wing Micro Aerial Vehicles

The morphological and kinematic parameters of bird wings are the result of natural selection and evolution, and the coordinated effect of these parameters enables birds to obtain excellent aerodynamic performance. The design of traditional FWMAVs generally analyzes and optimizes single morphological and kinematic parameters, which neglects the inherent connections between design variables and makes it difficult to achieve global optimal aerodynamic performance.

The geometric shape of a flapping wing can be described by its planform and airfoil shape, as shown in Fig 2. The study of the geometric shape of bird wings has a long history, dating back to the research of Norberg[3], Videler[4], Liu[5] and Bachman[6].

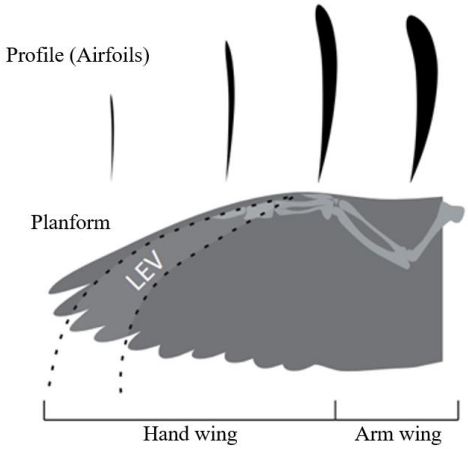


Figure 2 Typical plane shape of a bird's wing and profile shape at different stations along the span[7]

From a planar geometric perspective, the parameters of bird wing shape include wing area, aspect ratio, sweep angle, etc. Different shapes have significant effects on lift, drag, and thrust.

Regarding the planform geometry of flapping wings, the aerodynamic effects of parameters such as aspect ratio and sweep angle under static flight conditions have been obtained by conducting measurements and wind tunnel experiments on actual bird wing specimens[8][9]. By selecting real bird wing specimens for geometric measurements and wind tunnel experiments, the effects of aspect ratio and sweep angle on the lift and drag of flapping wings were studied at different angles of attack. The results show that wings with a large aspect ratio exhibit better low-drag performance by reducing induced drag; wings with a greater wingspan have a larger lift coefficient at small angles of attack; and wings with sweep have a larger lift coefficient at high angles of attack.

Additionally, the effects of wing aspect ratio and wing area distribution on flapping wing lift performance during hovering flight have been studied by constructing biomimetic flapping wing experimental models[10][11][12]. The results indicate that the aspect ratio significantly affects the strength and stability of the leading-edge vortex during hovering flapping flight, thereby having a significant impact on lift production. The effects of planform geometry parameters on the flow vortex structure and lift-thrust characteristics during forward flight state still warrant further exploration.

There is currently limited research on the influence of planform shape parameters on flapping flight, especially in the forward flight. Only a few studies have investigated the effects of aspect ratio on flapping thrust performance using symmetric airfoils and symmetric flapping modes. In 2018, numerical simulation results from Yuan Zongjing et al[13]. at Xi'an Jiaotong University showed that, in forward flight, the thrust performance of a NACA0012 flapping wing first increases and then decreases with increasing aspect ratio.

Flapping flight, as the direct source of propulsion for avian flight, is crucial for the formation of high lift and thrust during avian flight. The flapping pattern and rhythm play a key role in this process. Typical avian wing movements during flapping flight include flapping, twisting, sweeping, and folding[14][15][16][17]. Among them, flapping is the most fundamental form of motion, and the other movements contribute to different aerodynamic effects by being superimposed on flapping motion.

The mechanism of thrust generation during flapping was revealed by researchers through the study of unsteady motion of a two-dimensional airfoil[18][19][20]. Furthermore, the relationship between the direction and position of the wake vortex and the production of lift or drag by the airfoil has been confirmed through observations of the flow field[21] and experiments[22].

Research on the twisting motion of wings can be traced back to the pitching motion of a two-dimensional airfoil. On the one hand, the pitching motion of the airfoil generates a leading-edge vortex, which significantly increases lift. Furthermore, dynamic pitching motion enables the airfoil to maintain lift and continue to increase it even beyond the stall angle of attack[23]. On the other hand, excessive pitch angle can cause the leading-edge vortex to break off, resulting in a loss of lift[24]. The flapping and twisting motion of a three-dimensional wing can be simplified as the pitching and heaving motion of a two-dimensional airfoil. Research has shown that coupling the pitching motion with the heaving motion can result in significant changes in aerodynamic forces, and lead to larger thrust than either motion alone[25]. Additionally, the phase difference between the pitching and heaving motion also affects the lift and thrust performance, with a phase difference of around 90° achieving optimal propulsion efficiency[26]. In studies of the flapping motion of a three-dimensional wing modeled after a seagull[27], dynamic twisting motion was found to significantly improve the thrust and propulsion efficiency of flapping.

Recently, Wu et al.[28] utilizes the unsteady vortex lattice method (UVLM) to calculate the aerodynamic forces of flapping wings. Based on the DIRECT (rectangular partition) global optimization algorithm, the flapping motion parameters including flapping and twisting were iteratively optimized with a specific optimization objective of maximizing propulsion efficiency.

The sweeping motion of flapping wings was first studied by simplifying it as the front-to-back oscillation of an airfoil[29]. Researchers have studied the effects of kinematic parameters of sweeping motion on aerodynamic performance in a comprehensive manner. Researchers conducted numerical studies on the sweeping motion of the SG04 bird-inspired wing and found that forward sweep during the downstroke not only improves the propulsion efficiency of flying birds but also increases the thrust. Through numerical simulations, researchers have found that different motion trajectories have varying effects on the flow field structure of the NACA0012 airfoil[30][31]. Among these, they found that elliptical and fish-like motion patterns can significantly improve the propulsion efficiency of flapping wings. In addition, through experiments on the NACA0013 airfoil[32][33], researchers have also found that sweeping motion has a powerful aerodynamic force regulation function, which can increase the average lift or reduce lift oscillations. In the context of three-dimensional flapping, Koekkoek et al.[34] discovered in their study of a robotic bat wing that the angle between the flapping plane and the horizontal plane significantly affects the structure of the leading-edge vortex, indicating the significant role of sweeping motion in generating lift during flapping flight.

The folding motion of bird wings can lead to dynamic changes in wingspan. Through numerical simulations, the aerodynamic effects of spanwise folding have been studied[35], as well as the effects of different folding motion parameters on the performance of flapping wings[36]. It has been found that reducing span during the upstroke can decrease energy consumption and increase net lift, but it can have a detrimental effect on thrust. Additionally, folding motion alters the effective angle of attack and local tangential velocity, which affects the development of the wingtip leading-edge vortex and thus influences the lift generation of flapping wings.

Ke et al. used a revised quasi-steady aerodynamic model and hybrid genetic algorithm to perform the optimizations of wing geometry parameters and wing kinematic parameters to minimize the energy consumption of flapping wing hovering flight [37]. Although quasi-steady models can save computational resources, for the complex flapping and planar shapes of birds, CFD can more accurately calculate the flow field and aerodynamic forces.

In summary, researchers have used various motion patterns to investigate the aerodynamic effects of flapping wings. Heaving motion has been used to reveal the cause of thrust generation, while coupling heaving and pitching motion has been found to produce significant thrust. The study of sweeping motion has shown that it has a beneficial effect on both thrust and propulsion efficiency, and research on slow-flying birds has also found that it can increase lift, with the specific effect depending on the sweeping motion pattern. Dynamic changes in span through folding motion have been found to enhance lift. Although there are certain conclusions regarding the aerodynamic effects of each motion pattern, it is important to note that most studies have been conducted using simplified models or simplified motion patterns, which cannot fully reveal the mechanisms of motion interactions in the multi-degree-of-freedom motion of flapping wings.

On the other hand, there is a strong nonlinear coupling effect between the geometric design variables

and the motion design variables of flapping wings in optimizing objectives such as lift and thrust. If coupled optimization of both geometric and motion variables is performed, it requires the optimization method to have good global search capabilities. Currently, surrogate optimization methods have been widely used in the steady optimization of airfoils, wings, wing-body combinations, hypersonic vehicles, and rotors due to their high efficiency and global search capabilities in optimizing problems with hundreds of dimensions[38][39]. Therefore, combining surrogate optimization methods with unsteady NS equation aerodynamic modeling is an excellent choice for conducting the non-steady aerodynamic optimization of bird-inspired flapping wings that this article focuses on.
The purpose of this article is to construct a model that can simultaneously optimize both geometric and motion parameters, achieve global optimization of both geometric and motion parameters, and provide guidance for the design of flapping wings with complex planform shapes and motion degrees of freedom.

2.Methods

2.1Computational Fluid Dynamics (CFD)

2.2.1CFD solver

An in-house CFD solver, called ‘‘PMNS3DR”[40][41], is used in this work. The preconditioned Unsteady Reynolds Averaged Navier-Stokes (URANS) equations are solved based on a Finite Volume Method (FVM) within the framework of an efficient Full Approximation Storage (FAS) multigrid method. The space discretization is a cell-centered finite volume method using central difference, with nearly second-order accuracy on smooth structured grid. A dual time-stepping method is adopted for time marching and the LU-SGS scheme is implemented to accelerate the convergence for the inner iteration of pseudo-time stepping. SA turbulence model is adopted in this study to close the URANS equations.

2.2.2Dynamic overset grid technology for flapping wings

When the flapping wing moves in multiple degrees of freedom, the flapping wing produces large deformation, and it is difficult to generate a high computational accuracy using the dynamic mesh technique. The difficulty of mesh generation is reduced by using the nested mesh, which doesn't require the sub-domains to share boundaries. Nested meshes can avoid the problems of excessive mesh distortion and unreasonable mesh sparsity distribution for calculations with complex motions. Therefore, the grid system of "background grid + flapping wing grid" to construct the flapping wing computational grid is adopted in the paper, and the nested grid module for flapping wing multi-degree-of-freedom motion is developed, which is based on the autonomous program. The calculation flow is shown in Fig 3.

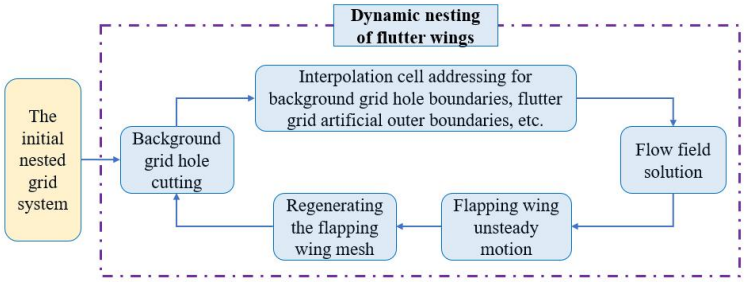


Figure 3 The nested solution process for the flapping motion

The key techniques in the process of numerical simulation of the flapping wing in this paper are described below, including the flapping wing motion model, the flapping wing computational grid generation method and the flapping wing computational grid dynamic nesting method.

A.Flapping motion mode

As shown in Fig 4, the typical motion of a flapping wing consists of flapping motion, chord-wise twisting motion and sweeping motion. The folding motion is produced, when the inner segment (arm wing) and outer segment (hand wing) of the flapping wing have different plunging motions. The stretching motion is formed, when the inner segment (arm wing) and outer segment (hand wing) of a flapping wing have different sweeping motions. In these movements, flapping motion is the most

basic form of flapping wing, which forms a variety of flapping motion by coupling other motions.

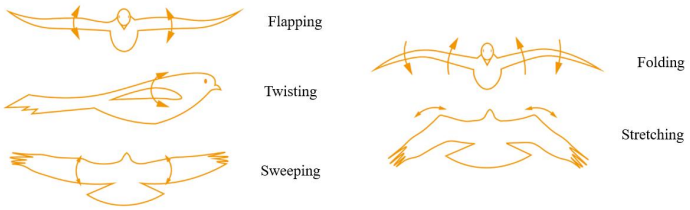


Figure 4 Typical macroscopic motion of a flapping wing

In this paper, the coupling of flapping motion and other motion is realized by customizing the unsteady motion module of flapping wing. The type of motion to be coupled is selected through the parameter file, and then the amplitude and phase of each motion are input into the motion parameter setting file to realize the flapping motion of the flapping wing with multiple degrees of freedom under the harmonic law.

B. Computational grid generation method for flapping wing

The grid system of "background grid + flapping wing grid" and the corresponding motion overset grid technology are adopted. As shown in Fig 5, the background grid adopts the orthogonalized Cartesian grid, and the whole grid is cuboid. In order to reduce the amount of calculation, only single-wing calculation is carried out. The surface of the background grid near the flapping wing root is the symmetric surface, which is set to be the symmetric boundary conditions. The other five surfaces are far field, which are set the far field boundary conditions, the distance of far field is not less than 30 times the chord length of the flapping wing. As shown in Fig 6, the background grid can be refined in the area near the flapping wing, especially in the wing root, wing tip and wake area according to the calculation requirements.

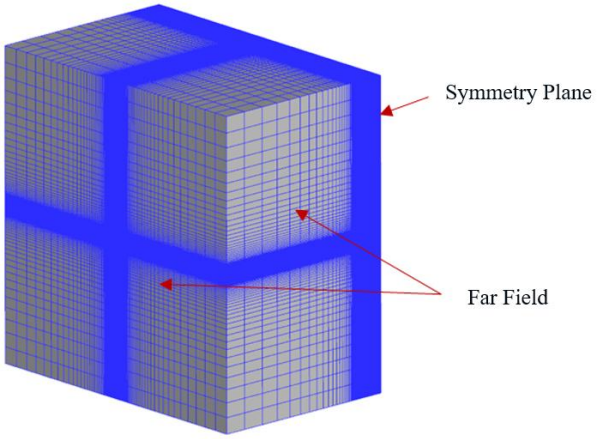
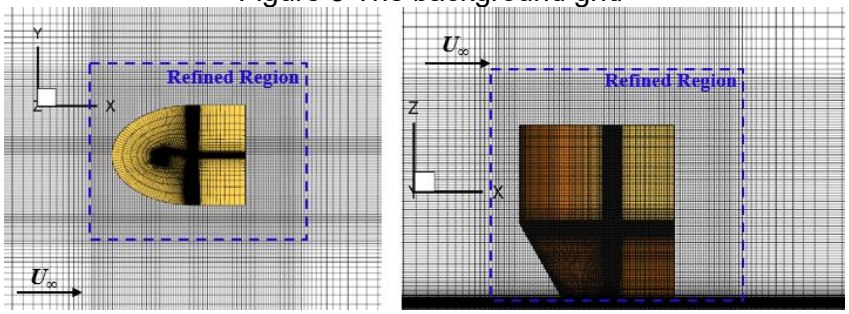


Figure 5 The background grid



（a）XY View （b）XZ View

Figure 6 Schematic diagram of background grid refinement zone

The surface mesh of the flapping wing is shown in Fig 7. For different shapes of the flapping wing, some specific parameters are used to control its surface topology and mesh density. Based on the

surface mesh of the flapping wing, the space C-H grid of the flapping wing is generated by the infinite interpolation method, as shown in Fig 8. The quality of the computational grid of the flapping wing is improved by increase the mesh number of the wingtip, wing root, leading edge, and trailing edge of the wing profile where the flow changes dramatically.

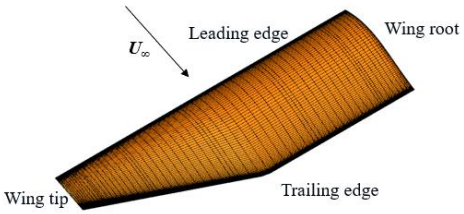


Figure 7 Schematic diagram of flapping wing surface mesh

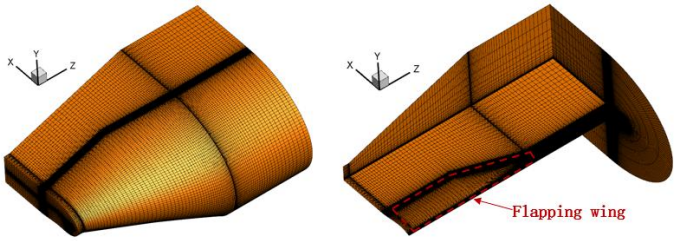


Figure 8 Schematic diagram of flapping wing volume mesh

The computing grid needs to be updated due to the position and shape of the flapping wing will change, during the flapping wing movement. In this paper, self-programming based on infinite interpolation method is used to update the flapping wing mesh, as shown in Fig 9. First of all, according to the shape of the flapping wing, the volume mesh at time $t = t_0$ is generated and taken as the reference grid. When the flapping wing moves to the time $t = t_i$, according to the flapping motion law, coordinate transformations are made on the volume mesh of the flapping wing at the time $t = t_0$ to obtain the surface mesh at the place $J = J_0$ (the first layer grid of the object surface normal) and $J = J_D$ (the far field grid of the object surface normal) at the time $t = t_i$ Then, based on the surface mesh of $J = J_0$ and $J = J_D$, the volume mesh of the flapping wing at time $t = t_i$ is generated by the infinite interpolation method. Compared with the method of obtaining the body mesh directly by coordinate transformation according to the flapping mode. In order to ensure the orthogonality of the normal mesh on the object surface of the flapping wing, the volume mesh updating strategy adopted, and generate high-quality body mesh during the flapping wing deformation.

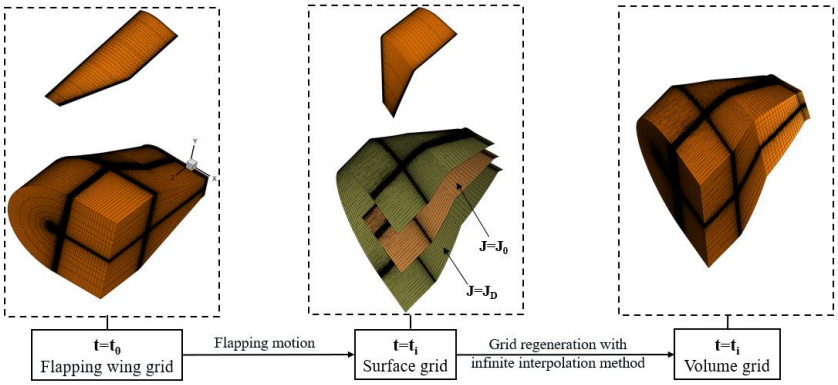


Figure 9 Dynamic mesh generation for flapping wing

As shown in Fig 10, the background grid and the flapping wing grid are combined to obtain the calculation system of "background grid + flapping wing grid". During the unsteady calculation, the background grid remained static, and the flapping wing grid has a customized multi-degree of freedom flapping motion relative to the background mesh. The whole grid system realizes the flow

variable interpolation between the background grid and the flapping wing grid at every physical time by the dynamic nesting relationship.

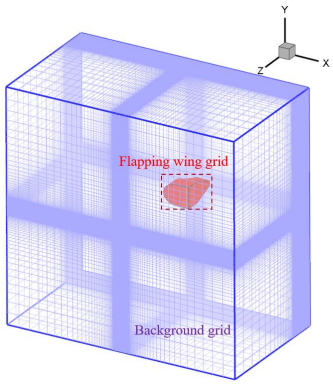


Figure 10 Background grid and flapping wing grid system

C. Dynamic overset method of computational mesh for flapping wing

In this paper, a trilinear interpolation method with high computational accuracy is used to interpolate the information between the contributing cells and the artificial boundary cells of the flapping grid system.

The grid cells in the nested grid system are classified into discretized cell, artificial boundary cells (including hole cell and artificial outer boundary cell), hole cell, and surface boundaries, which is identified in the program with the label IBK. All grid cells of the background grid and flapping wing grid are labeled as 1(IBK=1) before cell identification is performed. In the nested grid system, the background grid has hole cell and fringe cell in the area covered by the flapping wing grid, artificial outer boundary cell is existed on the outer boundary of the flapping wing grid, the flapping wing grid has surface boundaries on the flapping wing surface, and the background grid has far field boundaries and symmetry boundaries on the outer boundary. Discretized cell is points located inside the computational domain in the nested grid system, which is directly involved in the iterative solution of the flow field, with IBK=1 on the discretized cell. The hole cell is a convex closed region on the background grid that can contain the flapping wing and does not extend beyond the outer boundary of the flapping wing grid. The grid cells in this region don't participate in the flow field iterations and don't contribute interpolation information to the cells outside the hole, and the IBK=0 on the hole cell. The fringe cell is formed by artificially removing the hole cell from the background grid, and the flow variable values of the fringe cell need to be interpolated from the flapping wing grid cell overlapped with it, and the IBK=2 on the fringe cell. The artificial outer boundary cell is the outer boundary of the flapping wing grid, and the flow variable values of the artificial outer boundary cell is obtained by interpolation from the background grid cell overlapped with it, and the IBK=3 on the artificial outer boundary cell. The surfaces boundaries include far field boundaries, object plane boundaries, symmetry plane boundaries and so on, which can be handled in the conventional way.

During the flapping, the position of the flapping wing grid in the background grid changes all the time, so at each time step, new hole cell and fringe cell on the background grid need to be redetermined. The schematic diagram of the fringe cell formed by digging the background grid, as shown in Fig 11.

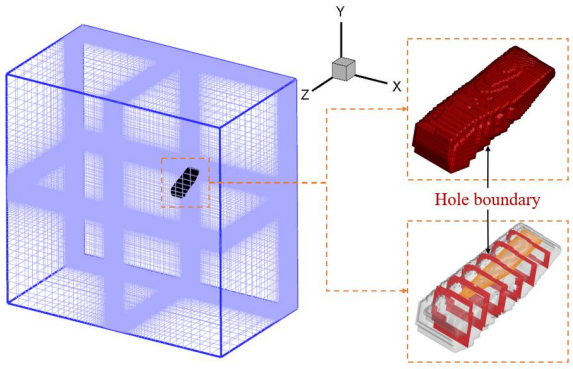


Figure 11 Hole boundary formed by digging holes in the background grid

The following steps are used to dig the hole and determine the hole boundary. First of all, a virtual closed body grid S is constructed based on the flapping wing grid, and the outer boundary Ω of the closed body is between the flapping wing surface grid and the outer boundary of the flapping wing body grid, and Ω completely wraps the flapping wing surface without exceeding the outer boundary. Then the "hole-digging" process is performed. For the background grid cell P, the distance reduction method[42]is used to search for the nearest virtual grid cell M in the virtual body grid S. If M is located in the region wrapped by Ω , the background grid cell P is recorded as a hole cell and the corresponding IBK= 0. Finally, the fringe cell is identified, and after the "digging" is finished, the grid cells is marked IBK=1, except the hole cell is marked IBK=0. If a cell F of the background grid has IBK=1 and there is cell with IBK=0 in its adjacent grid cells, then F is the cell on the first layer of the fringe and is marked as IBK=2. All cells with IBK=2 form the first layer of the fringe, and the number of layers of the fringe can be flexibly extended to the computational domain according to the demand of accuracy. The flow variable values of the fringe cells need to be interpolated from the flapping wing grid overlapping with them, and the flow variable values of the artificial outer boundary cells need to be interpolated from the background grid overlapping with them. The distance reduction method combined with the isoperimetric transformation can be used to find the interpolation contribution unit quickly. The nested grid requires that the flow parameters must match when passing the boundary during the flow field calculation, which can be achieved by interpolation methods. In this paper, trilinear interpolation method is used in the 3D calculation, as the following equation.

$$\phi = a_{c1} + a_{c2}\xi + a_{c3}\eta + a_{c4}\zeta + a_{c5}\xi\eta + a_{c6}\xi\zeta + a_{c7}\eta\zeta + a_{c8}\xi\eta\zeta \tag{1}$$

where ϕ is the variable to be interpolated, $0<\zeta<1$, $0<\eta<1$, $0<\xi<1$, $a_{cn}(n=1,...,8)$ are coefficients that depend on the values of the flow variables at the 8 vertices of the cube, as the Eq (2)

$$\begin{aligned}
a_{c1} &= \phi_1 \\
a_{c2} &= \phi_2 - \phi_1 \\
a_{c3} &= \phi_4 - \phi_1 \\
a_{c4} &= \phi_5 - \phi_1 \\
a_{c5} &= \phi_1 + \phi_2 + \phi_3 - \phi_4 \\
a_{c6} &= \phi_1 - \phi_2 - \phi_5 + \phi_6 \\
a_{c7} &= \phi_1 - \phi_4 - \phi_5 + \phi_8 \\
a_{c8} &= -\phi_1 + \phi_2 - \phi_3 + \phi_4 + \phi_5 - \phi_6 + \phi_7 - \phi_8
\end{aligned} \tag{2}$$

Trilinear interpolation can generally only be used on a cube, and the grid cell generated in curvilinear coordinates is a curved hexahedron, so when interpolating the flow variables at a point in the cell, the first step is to convert the curved hexahedron into a cube, which is generally done with an isoperimetric transformation. The correspondence between (ξ,ζ,η) and (x,y,z) is shown in Eq(3)

$$\begin{aligned}
x &= a_1 + a_2\xi + a_3\eta + a_4\zeta + a_5\xi\eta + a_6\xi\zeta + a_7\eta\zeta + a_8\xi\eta\zeta \\
y &= b_1 + b_2\xi + b_3\eta + b_4\zeta + b_5\xi\eta + b_6\xi\zeta + b_7\eta\zeta + b_8\xi\eta\zeta \\
z &= c_1 + c_2\xi + c_3\eta + c_4\zeta + c_5\xi\eta + c_6\xi\zeta + c_7\eta\zeta + c_8\xi\eta\zeta
\end{aligned} \tag{3}$$

where $a_n, b_n, c_n, n=1,...,8$ are the coordinate position coefficients of the vertices of the spatial curved hexahedron, which can be solved according to Eq (2). The (x,y,z) of the grid cell g within the cube is known. The corresponding (ξ,ζ,η) can be calculated from Eq (3) using Newton's iterative method. Finally, the values of the flow variables of the corresponding cell g can be obtained according to Eq (1)

2.2.3Accuracy verification of flapping wing numerical simulation program

In this section, the developed calculation procedure of flapping nested is verified by three flapping wings nonstationary motion arithmetic examples. The first and third example are both the cases of low Reynolds number, which are comparable to the scope of this paper. The first two examples are calculated by the RANS method (S-A model) and the last one is calculated by the hybrid RANS/LES method (SA-DDES).

A. The calculation example of heaving motion of NACA0012.

The first example is the flapping wing experiment conducted by Heathcote et al.[43] in a water tunnel in 2008. The experimental model is a rectangular wing with profile NACA0012, and the law of motion is heaving as shown in Eq(4) the experimental Reynolds number $Re=3\times10^4$.

$$H = 0.175c\cos(\omega t) \tag{4}$$

The geometric and kinematic parameters of the experimental model are shown in Table 1.

Table 1 The geometric and kinematic parameters of the experimental model

Parameter	Chord length c	Half stretch L	The amplitude of heaving H	The frequency of heaving ω	The velocity of free flow U	The density of free flow ρ
Value	0.1*m*	0.3*m*	0.0175*m*	10.92*rad/s*	0.3*m/s*	1000*kg/m*^{3}

The computing grid is shown in Fig 12. The background grid adopts Cartesian grid, and the grid number is 89×89×69. The flapping wing grid adopts CH grid, and the number of circumferential, normal, and stretch mesh points of the wing is 207×37×73, with a total mesh quantity of 1.1 million. The height of the first normal layer of the surface grid is 1.8×10-4c, ensuring that y+ is less than 1. \

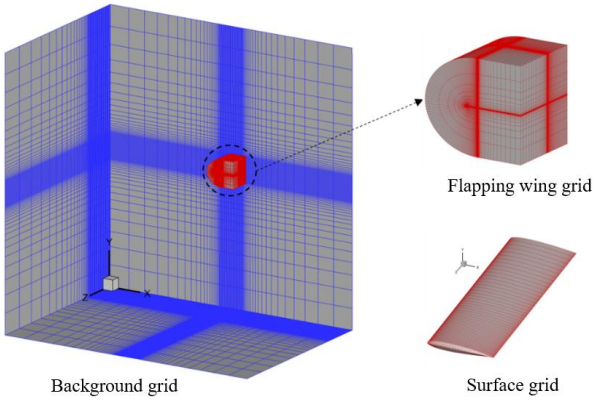


Figure 12 Calculation grid for NACA0012

The S-A turbulence model is used for calculation, and the calculation result is shown in Fig 13. Although the calculated thrust coefficient (C_T) of the flapping wing is different from the experimental value to some extent, compared with the calculation of Liu[44] and Lang[45], the calculation method adopted in this paper can better capture the phase of the two thrust peaks of the experimental results, which verifies the reliability of the numerical simulation method.

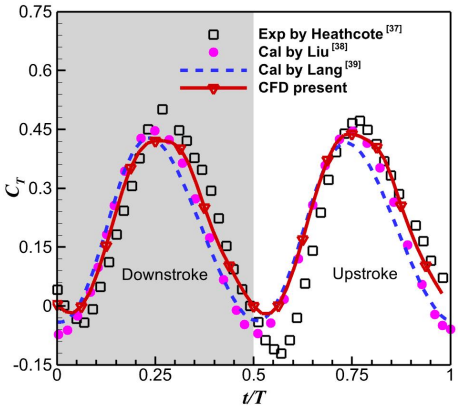


Figure 13 Comparison of computed and experimental values of instantaneous thrust coefficient CT

B. The calculation example of the plunge-twist coupling motion of NACA0014.

The calculation model is a rectangular wing with NACA0014 airfoil[46], and the ratio of wing half stretch to chord length is 4. The plunge-twist coupling motion is done by the wing with the following law of motion.

$$\psi(t) = \psi_m \cos(2\pi f \cdot t)$$
$$\alpha_{tip}(t) = \alpha_{tip,m} \cos(2\pi f \cdot t + \frac{\pi}{2}) \quad (5)$$

Where, $\psi(t)$ is the instantaneous plunging Angle, ψ_m is the amplitude of plunging Angle, $a_{tip}(t)$ is the instantaneous torsion Angle of the wing tip profile, $a_{tip,m}$ is the amplitude of the wing tip torsion Angle, f is the frequency. In this example, $\psi_m = 15^\circ$, $a_{tip,m} = 4^\circ$, and the reduced frequency *k=0.1*. The torsion Angle of wing root is 0, and the torsion Angle from wing root to wing tip is linearly distributed. The incoming flow velocity is *0.2353Ma*, and Re is 1 million based on the chord length.
As shown in Fig 14, the nested grid is used for calculation. The number of background grid is 89×89×69. The flapping wing grid number of circumferential, normal, and stretch mesh points of the wing is 241×41×105, with a total mesh quantity of 1.58 million. The height of the first normal layer of the surface grid is 3.6×10-5c, ensuring that y+ is less than 1.

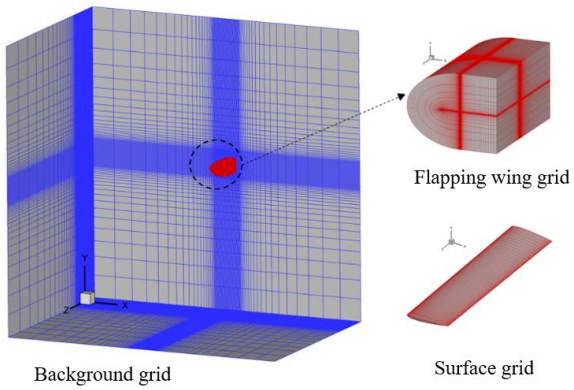


Figure 14 Calculation grid for NACA0014

The S-A turbulence model is used for calculation, and the calculation results is shown in Fig 15. The instantaneous lift coefficient (C_L) and differential pressure thrust coefficient ($(C_T)_p$) calculated are in good agreement with the references.

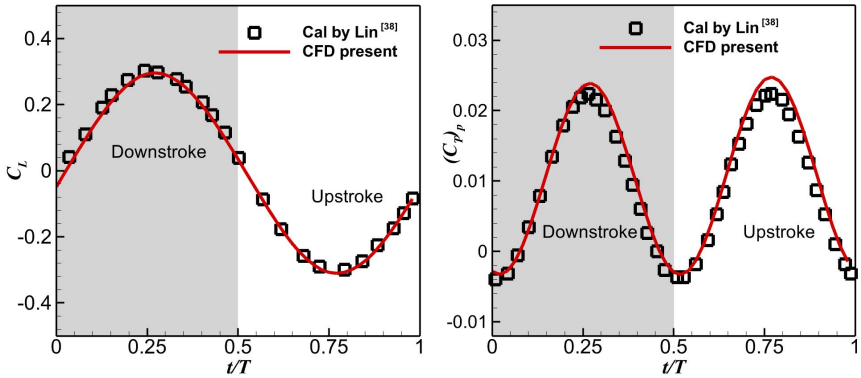


Figure 15 Comparison of computed instantaneous lift coefficient CL and pressure thrust coefficient (CT)p with reference literature results

C. Results and discussion

Birds have excellent flight capabilities and can adjust aerodynamic performance by changing the flapping motion of the wings. This paper conducts an unsteady aerodynamic optimization study of multi-degree-of-freedom flapping motion inspired by bird flight using surrogate models. First, a three-dimensional flapping wing motion aerodynamic optimization platform is built based on the surrogate optimization toolbox SurroOpt. Then, optimization design of flapping wing motion parameter is carried out using the developed platform to explore the optimal motion parameters for lift and thrust

performance, respectively. This provides references and guidance for the design and performance improvement of flapping wing aircraft inspired by birds at the same scale. In order to facilitate further analysis, this study parametrized the geometric shape and motion law of the flapping wing.

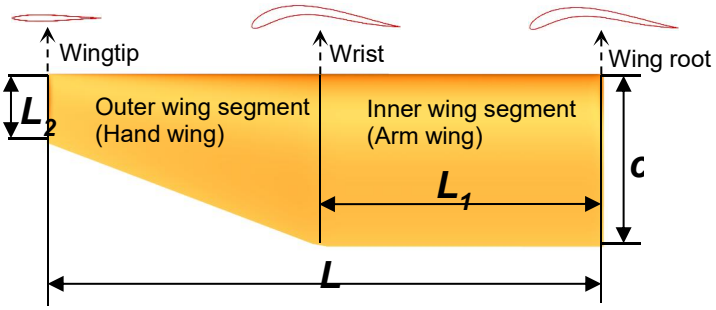


Figure 16 The planform and sectional shapes of a flapping wing

A flapping wing geometry model is established as shown in Figure 16. The flapping wing is divided into two segments, with the typical airfoil shapes shown in Figure 1 used for the wing root, wrist, and wing tip sections. The aspect ratio of the flapping wing is $L/c=3.6$ .The planform shape of the inner segment is rectangular, and its length accounts for the proportion L_1/L of the total length L .The planform shape of the outer segment is trapezoidal, with L_2 as the chord length of the wing tip. By adjusting parameters L_1 and L_2 , the length ratio of the inner and outer segments and the chord length of the wing tip can be changed comprehensively.

The motion pattern of the flapping wing is modeled based on the multi-degree-of-freedom motion of dove wings, neglecting the less obvious spanwise bending motion, and considering the coupled motion of flapping, twisting, and sweeping for the flapping wing. The inner segment of the wing has two degrees of freedom for flapping and twisting, while the outer segment follows the flapping and twisting motion of the inner segment, and also has dynamic twisting and front-back sweeping motion relative to the inner segment. The flapping wing has different time ratio of the downstroke Dr during the entire flapping cycle and is modeled using harmonic functions. The motion patterns of the wrist and wingtip during the downstroke and upstroke phases are given by equations , respectively.

When $t \le D_r \cdot T$:

$$\begin{aligned}
&\omega_1 = \pi/(D_r \cdot T)\\
&\phi_{wrist} = \phi_m \cos\omega_1 t\\
&\alpha_{wrist} = \alpha_0 + \alpha_{m1}\cos(\omega_1 t + \pi/2)\\
&\varphi_{wrist} = 0\\
&\phi_{tip} = \phi_m \cos\omega_1 t\\
&\alpha_{tip} = \alpha_{wrist} + \alpha_{m2}\cos(\omega_1 t + \pi/2)\\
&\varphi_{tip} = 0
\end{aligned} \tag{6}$$

When $D_r \cdot T \le t \le T$:

$$\begin{aligned}
&\omega_2 = \pi/((1-D_r)\cdot T)\\
&\phi_{wrist} = \phi_m \cos(\omega_2(t - D_r \cdot T) + \pi)\\
&\alpha_{wrist} = \alpha_0 + \alpha_{m1}\cos(\omega_2(t - D_r \cdot T) + \pi + \pi/2)\\
&\varphi_{wrist} = 0\\
&\phi_{tip} = \phi_m \cos(\omega_2(t - D_r \cdot T) + \pi)\\
&\alpha_{tip} = \alpha_{wrist} + \alpha_{m2}\cos(\omega_2(t - D_r \cdot T) + \pi + \pi/2)\\
&\varphi_{tip} = \varphi_{m2}\cos(\omega_2(t - D_r \cdot T) + \pi + \pi/2)
\end{aligned} \tag{7}$$

Where:

ω_1 and ω_2 :downstroke and upstroke angular velocities;

ϕ_{wrist} and ϕ_{tip} :wrist and wingtip flapping angles relative to the wing root;

ϕ_m :flapping angle amplitude, with ϕm=35° in this paper;

a_{wrist} and a_{tip} :wrist and wingtip twisting angles relative to the wing root;

a_0 :mean twisting angle, with α0=0 in this paper;

a_{m1} :wrist twisting angle amplitude relative to the wing root;

a_{m1} :wingtip twisting angle amplitude relative to the wrist;

φ_{wrist} and φ_{tip} :wrist and wingtip sweeping angles relative to the wing root and wrist, respective

φ_{m2} :wingtip sweeping angle amplitude relative to the wrist.

3.Results and discussion

3.1Thrust enhancement optimization for flapping wing

Firstly, thrust enhancement optimization is performed. The design of the flapping wing is mainly focused on the thrust design, and increasing the thrust of the flapping wing can compensate for the loss of lift in the design by increasing the flight speed. In this paper, the average thrust of the flapping wing is maximized as the optimization objective. During the optimization process, the average lift of the flapping wing is constrained to be no less than the value of the baseline wing, and the average power consumption is constrained to be no greater than the value of the baseline wing. Additionally, the static wing area of the flapping wing is not allowed to increase relative to that of the baseline wing. The constraints are used to obtain a flapping wing geometry and motion pattern that significantly improves the thrust performance while maintaining the same lift and wing area relative to the baseline wing, and without increasing power consumption. The calculation conditions are:*Re=5.6×104, U= 10 m/s, AoA=12º and f=8 Hz*, which is kept in consistant with the flight state of “Dove”. The mathematical model for the optimization problem is equations :

$$\begin{aligned} min \quad & -C_{T,mean} \\ s.t. \quad & C_{L,mean} \geq C_{L,mean,Baseline} \\ & C_{P,mean} \leq C_{P,mean,Baseline} \\ & S \leq S_{Baseline} \end{aligned} \tag{8}$$

The "Baseline" in this paper refers to the reference wing used for comparison in the optimization process. It represents the baseline wing with the following parameters: mean lift coefficient $C_{L,mean,Baseline}$*=0.92*, mean thrust coefficient $C_{T,mean,Baseline}$*=-0.139*, mean power coefficient $C_{P,mean,Baseline}$*=0.402*, static wing area $S_{Baseline}$*=3.06.*

The optimization process in this paper maintains the flapping angle of the flapping wing and optimizes the time ratio of the upstroke and downstroke, the twisting motion of the arm wing and hand wing, the sweeping motion of the hand wing relative to the arm wing, as well as the aspect ratio of the arm wing and the chord length of the wingtip, all at the same flapping angle. There are six design variables in total, including two geometric design variables and four motion law design variables. The geometric design variables are the ratio of the arm wing length to the wing span (L_1 / L) and the relative chord length of the wingtip (L_2 / c). The motion law design variables are the time ratio of the downstroke (*Dr*), the twisting amplitude angle of the wrist relative to the wing root (a_{m1}), the twisting amplitude angle of the wingtip relative to the wrist (a_{m2}), and the sweeping amplitude angle of the wingtip relative to the wrist (φ_{m2}). The optimization design space is shown in Table 2.

Table 2 Optimization design variables and the ranges

Design variable	L_1/L	L_2/c	D_r	$a_{m1}(^\circ)$	$a_{m2}(^\circ)$	$\varphi_{m2}(^\circ)$
Lower bound	0.333	0.10	0.35	0	0	0

Upper bound	0.666	0.55	0.65	25	25	45

The initial sample points were set to 30, obtained using Latin hypercube sampling. The optimization was performed using a surrogate-based optimization algorithm. The convergence curve of the optimization is shown in Figure 17, and the optimization process required 100 CFD calls to obtain the optimized solution.

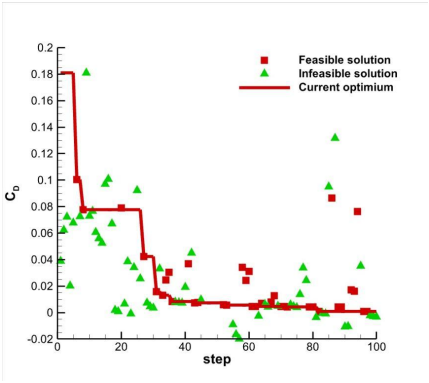


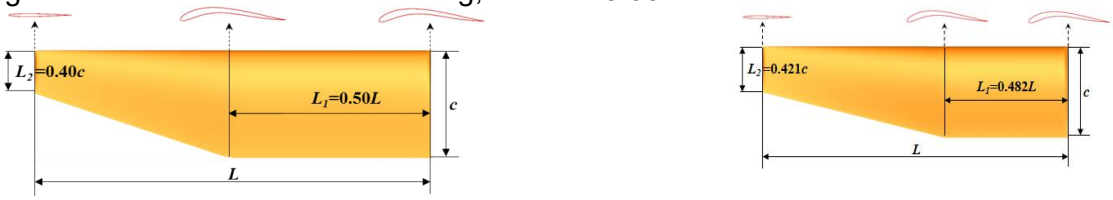
Figure 17 Convergence curve of optimization

Table 3 presents a comparison of design variables and aerodynamic performance between the baseline wing (*Baseline*) and the optimized wing (*Opt*). After optimization, with the constraints on mean lift coefficient $C_{L,mean}$, mean power coefficient $C_{P,mean}$, and static geometric area S of the flapping wing fulfilled, the mean thrust coefficient $C_{T,mean}$ of the optimized wing was increased from -0.139 of the baseline wing to -0.001 (equivalent to an increase in thrust of 17.8 g per wing), resulting in a significant improvement in the thrust performance of the flapping wing.

Table 3 Comparison of design variables and aerodynamic performance between the baseline wing (Baseline) and the optimized wing (Opt)

Design variable	L_1/L	L_2/c	D_r	$a_{m1}(^\circ)$	$a_{m2}(^\circ)$	$\varphi_{m2}(^\circ)$
Baseline	0.5	0.4	0.5	0	0	0
Opt	0.482	0.421	0.560	11.4	21.8	20.1
Design variable	S/c^2	$C_{L,mean}$	$C_{T,mean}$	$C_{P,mean}$	η_L	η_T
Baseline	3.06	0.92	-0.139	0.402	2.28	-0.345
Opt	3.06	0.92	-0.001	0.223	5.14	-0.0056

Figure 18 shows a comparison of the static geometric shapes of the baseline wing and the optimized wing. Compared to the baseline wing, the optimized wing has an increased chord length of the wingtip, from 0.4c to 0.421c, a decreased length of the arm wing, from 0.50L to 0.482L and the same static geometric area as the baseline wing, which is 3.06.



(a)baseline (b)Opt

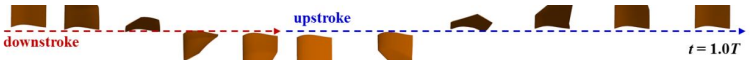
Figure 18 Comparison of static geometric shapes between the baseline wing (Baseline) and the optimized wing (Opt)

Figure 19 shows the dynamic geometric shapes and flapping motion of the baseline wing and the optimized wing. After the thrust-increasing optimization, the optimized wing has a slightly increased time ratio of the downstroke compared to the baseline wing. The optimized wing exhibits significant dynamic twisting motion throughout the flapping cycle, with the flapping wing tilting down and twisting during the downstroke, and tilting up and twisting during the upstroke. Different to the baseline wing, the optimized wing has sweeping motion of the arm wing relative to the hand wing,

namely the flapping wing perform expansion-contraction motion.



(a)Baseline geometry and motion



(b)Optimized geometry and motion

Figure 19 Comparison of dynamic geometric shapes and flapping motion between the baseline wing and the optimized wing

Figure 20 shows the dynamic geometric shapes and flapping motion of the baseline wing and the optimized wing. After the thrust-increasing optimization, the optimized wing has a slightly increased time ratio of the downstroke compared to the baseline wing. The optimized wing exhibits significant dynamic twisting motion throughout the flapping cycle, with the flapping wing tilting down and twisting during the downstroke, and tilting up and twisting during the upstroke. Different to the baseline wing, the optimized wing has sweeping motion of the arm wing relative to the hand wing, namely the flapping wing perform expansion-contraction motion.

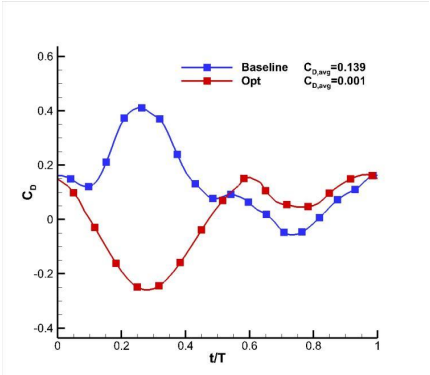
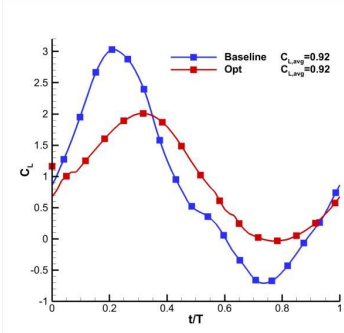
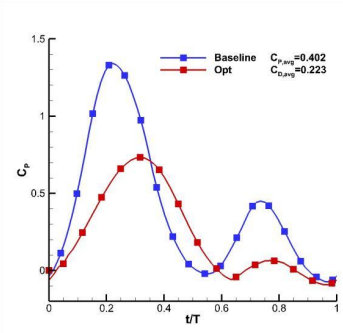


Figure 20 Comparison of instantaneous thrust coefficients CT between the baseline wing (Baseline) and the optimized wing (Opt)

Figure 21 shows the variation of instantaneous lift coefficient CL and instantaneous power coefficient CP between the optimized wing and the baseline wing. In terms of the instantaneous lift coefficient, the optimized wing exhibits a decrease in angle of attack and a decrease in the peak value of the instantaneous lift coefficient during the downstroke due to the tilting and twisting motion, while an increase in angle of attack and an increase in the valley value of the instantaneous lift coefficient during the upstroke due to the tilting and twisting motion. Since the twisting has completely opposite effects on the instantaneous lift in the downstroke and upstroke, the optimized wing can achieve a significant increase in mean thrust coefficient while satisfying the constraint that the mean lift coefficient should not decrease relative to the baseline wing. In terms of the instantaneous power coefficient, the optimized wing exhibits a significant decrease in the peak value of the instantaneous positive lift load during the downstroke and the peak value of the instantaneous negative lift load during the upstroke due to the twisting motion, resulting in a decrease in the peak values of the instantaneous power consumption for both the downstroke and upstroke. Consequently, the mean power consumption of the optimized wing is significantly reduced compared to the baseline wing.





(a) Instantaneous lift coefficient C_L (b) Instantaneous power coefficient C_P

Figure 21 Comparison of instantaneous lift coefficient CL and instantaneous power coefficient CP between the baseline wing (Baseline) and the optimized wing (Opt)

3.2 Lift enhancement optimization for flapping wing

This study aims to maximize the mean lift coefficient of the flapping wing, with constraints on the mean thrust coefficient not being less than that of the baseline wing, the mean power consumption not being greater than that of the baseline wing, and the static wing area of the flapping wing not increasing relative to that of the baseline wing. The optimization conditions are: $R_e = 5.6\times10^4$, $U = 10m/s$, and $f = 8Hz$. The mathematical model for the optimization problem is Eq (9):

$$\begin{aligned} min \quad & -C_{L,mean} \\ s.t. \quad & C_{T,mean} \geq C_{T,mean,Baseline} \\ & C_{P,mean} \leq C_{P,mean,Baseline} \\ & S \leq S_{Baseline} \end{aligned} \tag{9}$$

The baseline wing, optimized design variables, and design space used in this study are consistent with the previous section and will not be repeated here. The initial sample points for optimization were set to 30 and obtained using Latin hypercube sampling. A surrogate optimization algorithm was used for optimization. The convergence curve of the optimization is shown in Figure 22, and a total of 85 CFD calls were made to obtain the optimized solution.

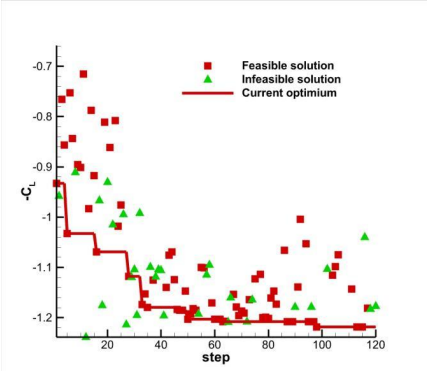


Figure 22 Convergence curve of optimization

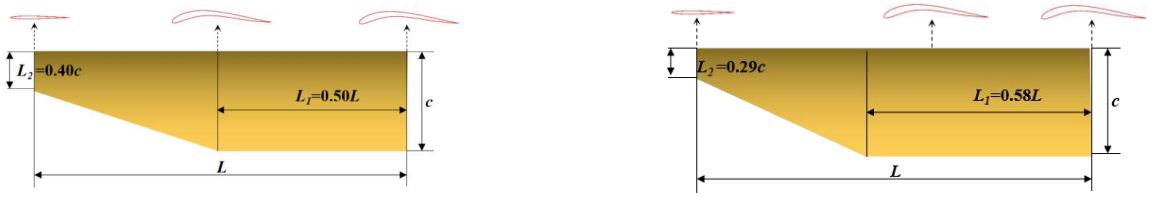
Table 4 shows a comparison of the design variables and aerodynamic performance between the baseline wing and the optimized wing. After optimization, the optimized wing satisfies the constraints on the mean thrust coefficient CT,mean, mean power coefficient CP,mean, and static geometric area S of the flapping wing, and the mean lift coefficient CL,mean is increased from 0.92 of the baseline wing to 1.22 (equivalent to an increase in lift of 38.1g for a single wing), resulting in a 32.6% improvement in mean lift performance. The lift performance of the flapping wing is significantly improved.

Table 4 Comparison of design variables and aerodynamic performance between the baseline wing (Baseline) and the optimized wing (Opt)

Design variable	L_1/L	L_2/c	D_r	$a_{m1}(^\circ)$	$a_{m2}(^\circ)$	$\varphi_{m2}(^\circ)$
Baseline	0.5	0.4	0.5	0	0	0
Opt	0.57	0.29	0.36	16.7	25	20.1
Design variable	**S/c^2**	**$C_{L,mean}$**	**$C_{T,mean}$**	**$C_{P,mean}$**	**η_L**	**η_T**
Baseline	3.06	0.92	-0.139	0.402	2.28	-0.345
Opt	3.06	1.22	-0.079	0.210	5.81	-0.376

Figure 23 shows a comparison of the static geometric shapes between the baseline wing and the optimized wing. Compared with the baseline wing, the optimized wing has an increased wingtip chord length, from 0.4c to 0.501c, and a increased arm wing length, from 0.50L to 0.58L, while the static geometric area of the optimized wing is equal to that of the baseline wing, at 3.06. It is worth

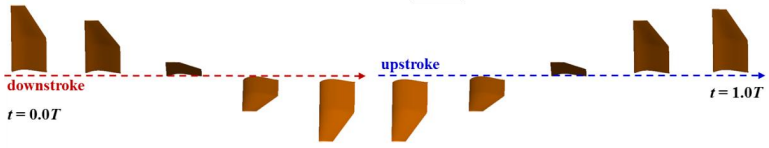
noting that the static geometric shape of the flapping wing obtained by lift-increasing optimization in this study is very similar to that obtained by thrust-increasing optimization in the previous section. The lift or thrust increase of the flapping wing is mainly achieved by changing the flapping motion law, which is consistent with the phenomenon that birds in nature often adjust their aerodynamic forces by changing their motion laws. This indicates that the optimization results in this study are reasonable.



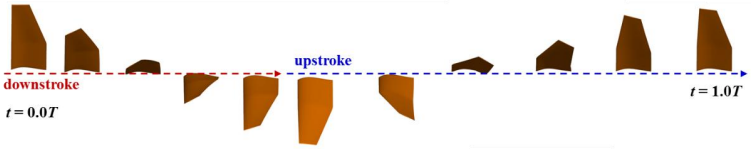
(a)baseline (b)Opt

Figure 23 Comparison of the static geometric shapes between the baseline wing (Baseline) and the optimized wing (Opt)

Figure 24 shows the dynamic geometric shapes and flapping motion laws of the baseline wing and the optimized wing. After lift-increasing optimization, compared with the baseline wing, the optimized wing has a significantly reduced downstroke time ratio. The optimized wing undergoes obvious dynamic twisting motion throughout the flapping cycle, with the flapping wing tilting downward and twisting during the downstroke, and tilting upward and twisting during the upstroke. In addition, during the upstroke phase, the arm wing of the optimized wing undergoes a sweeping motion relative to the hand wing, that is, there is a flexion-extension motion during the flapping process.



(a) Baseline geometry and motion



(b) Optimized geometry and motion

Figure 24 Comparison of dynamic geometric shapes and flapping motion between the baseline wing (Baseline) and the optimized wing (Opt)

Figure 25 shows a comparison of the instantaneous lift coefficient CL between the optimized wing and the baseline wing. It can be seen that the significant reduction in the instantaneous negative lift coefficient during the upstroke phase is the main reason for the increase in mean lift coefficient of the optimized wing. Compared with the baseline wing, the optimized wing has three main reasons for the reduction in instantaneous negative lift during the upstroke phase. Firstly, the optimized wing has obvious flexion-extension motion during the upstroke phase, which can reduce the negative lift of the flapping wing. Secondly, the downstroke time ratio of the optimized wing is small, which means that the upstroke time of the flapping wing is long, equivalent to a decrease in upstroke frequency, resulting in a reduction in the instantaneous negative lift of the flapping wing. Thirdly, the optimized wing has a large upward tilting motion during the upstroke phase. Although the coupling flexion-extension motion will reduce the lift-increasing effect of the upward tilting motion, it can still improve the instantaneous lift of the optimized wing during the upstroke phase to a certain extent.

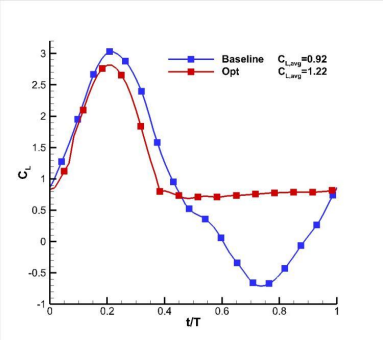
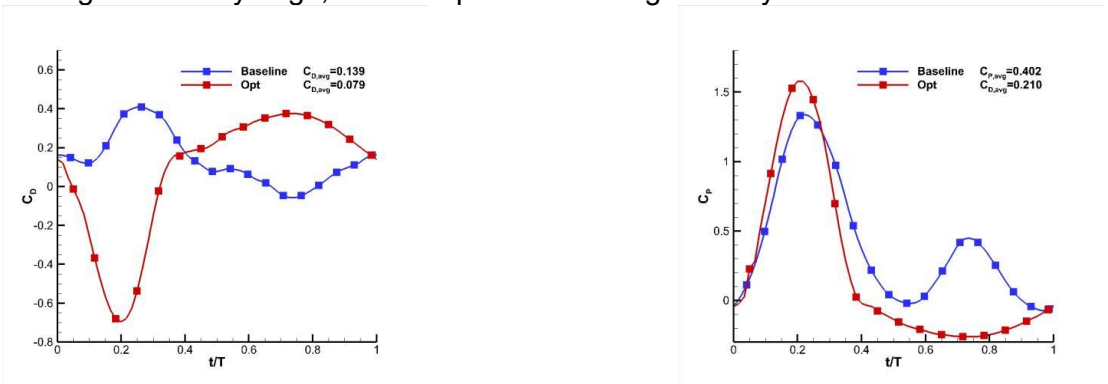


Figure 25 Comparison of instantaneous thrust coefficients CL between the baseline wing (Baseline) and the optimized wing (Opt)

Figure 26 shows the variations in the instantaneous thrust coefficient CT and instantaneous power coefficient CP between the baseline wing and the optimized wing. With regard to thrust, due to the significant change in the motion pattern, the thrust characteristics of the optimized wing are completely different from those of the baseline wing. The larger downward tilting motion and smaller downstroke time ratio of the optimized wing result in a larger thrust peak during the downstroke phase, while the baseline wing has a thrust peak during the upstroke phase. Although there is a large difference in the instantaneous thrust coefficient between the optimized wing and the baseline wing, their mean thrust coefficients are not significantly different, with the mean thrust of the optimized wing being slightly smaller at the wingtip compared to the baseline wing. With regard to aerodynamic power, the downstroke power peak of the optimized wing is higher than that of the baseline wing, while the upstroke power peak is lower. Because the upstroke time ratio of the optimized wing is relatively large, its mean power is still significantly reduced.



(a) Instantaneous thrust coefficient C_T (b) Instantaneous power coefficient C_P

Figure 25 Comparison of the instantaneous thrust coefficient CT and instantaneous power coefficient CP between the baseline wing (Baseline) and the optimized wing (Opt)

4.Conclusions

In this paper, based on the generalized surrogate optimization toolbox "SurroOpt" and the multi-degree-of-freedom numerical solver for flapping wings developed in this study, a three-dimensional aerodynamic optimization platform coupling the geometric shape and motion laws of flapping wings was constructed. On this basis, aerodynamic optimization design was carried out for a typical two-stage flapping wing, and the main content and conclusions are as follows.

Coupled optimization of the geometric shape and motion laws of the flapping wing was carried out, and ultimately a flapping wing with an average thrust coefficient increase of 0.138 (equivalent to an increase in thrust of 17.8 g per wing)was obtained, while ensuring that the mean lift coefficient was not less than that of the baseline wing, the mean power consumption was not greater than that of the baseline wing, and the wing area was unchanged relative to the baseline wing. The increase in mean thrust coefficient of the flapping wing was mainly due to the larger downward tilting and twisting motion during the downstroke.

Coupled optimization of the geometric shape and motion laws of the flapping wing was carried out, and ultimately a flapping wing with a 32.6%improvement in lift performance(equivalent to an increase

in lift of 38.1g for a single wing) was obtained, while ensuring that the mean thrust coefficient was not less than that of the baseline wing, the mean power consumption was not greater than that of the baseline wing, and the wing area was unchanged relative to the baseline wing. The static geometric shape of the flapping wing obtained from lift-increasing optimization is very close to that obtained from thrust-increasing optimization. The flapping wing mainly adjusts from large thrust to large lift by changing its motion. In lift-increasing optimization, the improvement in lift performance of the optimized wing is mainly due to the coupling of the upward tilting and twisting motion during the upstroke phase with the longer upstroke time.

5.Copyright Statement

The authors confirm that they, and/or their company or organization, hold copyright on all of the original material included in this paper. The authors also confirm that they have obtained permission, from the copyright holder of any third party material included in this paper, to publish it as part of their paper. The authors confirm that they give permission, or have obtained permission from the copyright holder of this paper, for the publication and distribution of this paper as part of the ICAS proceedings or as individual off-prints from the proceedings.

References

[1] Yang W Q, Song B F, Song W P, et al. The effects of span-wise and chord-wise flexibility on the aerodynamic performance of micro flapping-wing[J]. Chinese Science Bulletin, 2012, 57(22): 2887-2897.

[2] Keennon, M., Klingebiel, K. and Won, H. 2012. “Development of the nano hummingbird: a tailless flapping wing micro air vehicle.” In: 50th AIAA Aerospace Sciences Meeting Including the New Horizons Forum and Aerospace Exposition, Nashville, Tennessee.

[3] Norberg U M. Vertebrate Flight: Mechanics, Physiology, Morphology, Ecology, and Evolution [M]. Berlin: Springer, 1990, 1-5.

[4] Videler, J. J. , E. J. Stamhuis , and G. D. E. Povel . "Leading-Edge Vortex Lifts Swifts." Science, Vol. 306, No. 5703, 2004, pp. 1960, 1962.

[5] Liu, T. , et al. "Avian Wing Geometry and Kinematics." Aiaa Journal Vol. 44, No. 5, 2006, pp. 954, 963.

[6] Bachmann T. Anatomical, morphometrical and biomechanical studies of barn owls’ and pigeons’ wings[D]. Aachen: RWTH Aachen University, 2010.

[7] Thielicke, W. , and E. Stamhuis . "The influence of wing morphology on the three-dimensional flow patterns of a flapping wing at bird scale." Journal of Fluid Mechanics Vol. 768, 2015, pp. 240, 260.

[8] Lees J J, Dimitriadis G, Nudds R L. The influence of flight style on the aerodynamic properties of avian wings as fixed lifting surfaces[J]. Peer J, 2016, 4: e2495.

[9] Van Oorschot B K , Mistick E A , Tobalske B W. Aerodynamic consequences of wing morphing during emulated take-off and gliding in birds[J]. Journal of Experimental Biology, 2016, 219: 3146-3154.

[10]Phillips N , Knowles K , Bomphrey R J. The effect of aspect ratio on the leading-edge vortex over an insect-like flapping wing[J]. Bioinspiration & Biomimetics, 2015, 10(5): 056020.

[11]Fu J , Liu X , Shyy W, et al. Effects of flexibility and aspect ratio on the aerodynamic performance of flapping wings[J]. Bioinspiration & Biomimetics, 2018, 13: 036001.

[12]Shahzad A, Mumtaz Qadri M N, Ahmad S. Numerical analysis of high aspect ratio flexible wings in flapping motion[J]. Journal of Applied Fluid Mechanics, 2019, 12: 1979-1988.

[13]YUAN Zongjing, HAN Jiakun, CHEN Gang. Investigation on the influence of aspect ratio on the thrust performance of bionic motion wing under low Reynolds number[J]. ACTA AERODYNAMICA SINICA, 2018, 36(1): 156-162.

[14]Berg A M, Biewener A A. Wing and body kinematics of takeoff and landing flight in the pigeon (Columba livia)[J]. Journal of Experimental Biology, 2010, 213: 1651-1658.

[15]Carruthers A C, Thomas A L R, Taylor G K. Automatic aeroelastic devices in the wings of a steppe eagle Aquila nipalensis[J]. Journal of Experimental Biology, 2007, 210: 4136-4149.

[16]Ros I G, Bassman L C, Badger M A, et al. Pigeons steer like helicopters and generate down and upstroke lift during low speed turns[J]. Proceedings of the National Academy of Sciences of the United States of America, 2011, 108: 19990-19995.

[17]Chin D D, Lentink D. Flapping wing aerodynamics: From insects to vertebrates[J]. Journal of Experimental Biology, 2016, 219: 920-932.

[18]Knoller R. Die Gesetze des Luftwiderstandes (The Laws of Wind Resistance)[J]. Flug-und Motortechnik (Wien), 1909, 3(21): 1-7.

[19]Betz A. Ein beitrag zur erklaerung segelfluges[J]. Z Flugtech Motorluftschiffahrt, 1912, 3: 269-272.

[20]Katzmayr R. Effect of periodic changes of angle of attack on behavior of airfoils[J]. Technical Report Archive & Image Library, 1922.

[21]Von Karman T, Burgers J M. Aerodynamic Theory [C]. Berlin: Springer, 1934, 1-5.

[22]Bratt J B. Flow patterns in the wake of an oscillating airfoil [R]. Aeronautical Research Council R&M, 1953, 2773.

[23]Ekaterinaris J A, Platzer M F. Computational prediction of airfoil dynamic stall[J]. Progress in Aerospace Sciences, 1998, 33(11): 759-846.

[24]Gharali K, Johnson D A. Dynamic stall simulation of a pitching airfoil under unsteady freestream velocity[J]. Journal of Fluids and Structures, 2013, 42: 228-244.

[25]Yu M, Wang Z J, Hu H. High fidelity numerical simulation of airfoil thickness and kinematics effects on flapping airfoil propulsion[J]. Journal of Fluids and Structures, 2013, 42:166-186.

[26]Koochesfahani M M. Vortical patterns in the wake of an oscillating airfoil[J]. AIAA Journal, 1989, 27(9): 1200-1205.

[27]Chang X H, Zhang L P, Ma R, et al. Numerical investigation on aerodynamic performance of a bionic flapping wing[J]. Applied Mathematics and Mechanics, 2019, 40(11): 1625-1646.

[28]WU Yue, XIE Changchuan, YANG Chao, et al. Optimal design of motion parameters of flapping wing[J]. Journal of Beijing University of Aeronautics and Astronautics, 2022, 48(7): 1324-1331. doi: 10.13700/j.bh.1001-5965.2021.0593(in Chinese)

[29]Bansmer S E , Radespiel R. Flapping flight: high thrust andpropulsive efficiency due to forward gliding oscillations[J]. AIAA Journal, 2012, 50(12):2937-2942.

[30]Esfahani J A, Barati E, Karbasian H R. Fluid structures of flapping airfoil with elliptical motion trajectory[J]. Computers & Fluids, 2015; 108: 142-55.

[31]Karbasian H R, Esfahani J A. Enhancement of propulsive performance of flapping foil by fish-like motion pattern[J]. Computers & Fluids, 2017; 156: 305-16.

[32]Triantafyllou M S. Adding in-line motion and model-based optimization offers exceptional force control authority in flapping foils[J]. Journal of Fluid Mechanics, 2014; 742: 5-34.

[33]Izraelevitz J S, Kotidis M P, Triantafyllou M S. Optimized kinematics enable both aerial and aquatic propulsion from a single three-dimensional flapping wing[J]. Physical Review Fluids, 2018; 3(7): 073102.

[34]Koekkoek G, Muijres F T, Johansson L C, et al. Stroke plane angle controls leading edge vortex in a bat-inspired flapper[J]. Comptes Rendus Mecanique, 2012, 340(1-2): 0-106.

[35]Bahlman J W, Swartz S M, Breuer K S. How wing kinematics affect power requirements and aerodynamic force production in a robotic bat wing[J]. Bioinspiration & Biomimetics, 2014, 9(2):025008.

[36]Lang X Y, Song B F, Yang W Q, et al. Effect of spanwise folding on the aerodynamic performance of three dimensional flapping flat wing[J]. Physics of Fluids, 2022, 34, 021906.

[37]Ke, X., et al., Wing geometry and kinematic parameters optimization of flapping wing hovering flight for minimum energy. Aerospace Science and Technology, 2017. 64(Supplement C): p. 192-203.

[38]Han Z H, Chen J, Zhang K S, et al. Aerodynamic Shape Optimization of Natural-Laminar-Flow Wing Using Surrogate-Based Approach[J]. AIAA Journal, 2018, 56(7): 2579-2593.

[39]Liu F, Han Z H, Zhang Y, et al. Surrogate-Based Aerodynamic Shape Optimization of Hypersonic Flows Considering Transonic Performance[J]. Aerospace Science and Technology, 2019, 93(10): 105345.

[40]Xie F, Song WP, Han ZH. Numerical study of high-resolution scheme based on preconditioning method[J]. Journal of Aircraft, 2008, 46 (2): 520-534.

[41]Han ZH, He F, Song WP, et al. A preconditioned multigrid method for efficient simulation of three dimensional compressible and incompressible flows[J]. ChineseJournal of Aeronautics, 2007; 20(4): 289–96.

[42]杨文青, 宋笔锋, 宋文萍. 高效确定重叠网格对应关系的距离减缩法及其应用. 航空学报, 2009, 30(2):205-212.

[43]Heathcote S, Wang Z, Gursul I. Effect of spanwise flexibility on flapping wing propulsion[J]. Journal of Fluids and Structures, 2008, 24(2): 183-199.

[44]Liu H. Integrated modeling of insect flight: From morphology, kinematics to aerodynamics[J]. Journal of Computational Physics, 2009, 228(2): 439-459.

[45]稂鑫雨. 仿鸟扑翼三维复杂扑动流场特性数值模拟[D]. 西北工业大学, 2018, 50-52.

[46]Lin S Y, Hu J J. Numerical study of flapping wing[C]. Aiaa Fluid Dynamics Conference & Exhibit. 2003.

[47]Lee T, Gerontakos P. Investigation of flow over an oscillating airfoil[J]. Journal of Fluid Mechanics, 2004, 512:313-341.

[48]Li X, Feng L H, Li ZY. Flow mechanism for the effect of pivot point on the aerodynamic characteristics of a pitching airfoil and its manipulation[J]. Physics of Fluids, 2019, 31(8): 087108.

[49]Kim Y, Xie Z T. Modelling the effect of freestream turbulence on dynamic stall of wind turbine blades[J]. Computers & Fluids, 2016, 129: 53–66.

[50]年鹏. 仿鸟类扑翼飞行器设计中的关键问题研究[D]. 西北工业大学, 2021, 23-27.

[51]Han Z H. SurroOpt: a generic surrogate¬based optimization code for aerodynamic and multidisciplinary design[C]. in: 30th Congress of the International Council of the Aeronautical Sciences: 0281. Daejeon, South Korea, 2016.

[52]Han Z H, Zhang K S. Surrogate-based optimization[M]. InTech Book, 2012: 343-362.

[53]Han Z H, Goertz S. A hierarchical Kriging model for variable-fidelity surrogate modeling [J]. AIAA Journal, 2012, 50(3): 1885-1896.

[54]Han Z H, Zimmermann R, Goertz S. An alternative CoKriging model for variablefidelity surrogate modeling [J]. AIAA Journal, 2012, 50(5): 1205-1210.

[55]刘俊.基于代理模型的高效气动优化设计方法及应用[D]. 西北工业大学, 2015.